Petroleum Science 23 (2026) 4320–4335

Contents lists available at ScienceDirect

Petroleum Science

journal homepage: www.keaipublishing.com/en/journals/petroleum-science

Original Paper

# Failure mechanism and structure optimization of sand control screen in water-bearing gas well

Fu-Cheng Deng [a,d,*], Jun Gong [a], Ning Gong [c], Yao-Tu Han [c], Yi-Mou Li [b]

[a] College of Mechanical Engineering, Yangtze University, Jingzhou, 434000, Hubei, China
[b] Sinopec Northwest Oilfield Company, Urumqi, 830011, Xinjiang, China
[c] China National Offshore Oil Corporation, Tianjin Branch, Tianjin, 300459, China
[d] Guangzhou Institute of Energy Conversion, Chinese Academy of Sciences, Guangzhou, 510640, Guangdong, China

ARTICLE INFO

*Article history:*
Received 8 April 2025
Received in revised form
9 October 2025
Accepted 14 December 2025
Available online 18 December 2025

Edited by Min Li

*Keywords:*
Water producing gas well
Sand screen erosion
Computational fluid dynamics (CFD)
Erosion mechanism model
Structural optimization

ABSTRACT

The prospect of natural gas reservoir is broad. As the mining channel, the state of gas well determines the mining efficiency of the whole natural gas reservoir. After long-term mining of gas wells, the problem of water production will lead to the destruction of sand control screens, resulting in a large amount of sand production, which seriously endangers the safe production of gas wells. The "punched seam sleeves (PSS) + metal woven meshes (MWM)" is the main sand control structure, which failure mechanism needs to be explored. In this study, based on the erosion and corrosion environment, a simulation test with water content and gas production rate as single factor variables was designed. The dynamic grid layer laying method was used to simulate the corrosion environment, and the influence of erosion wear on sand control failure of screen pipe in water-bearing gas well under corrosive environment is analyzed. Through multi-factor comparison and evaluation, the structure of the screen pipe was optimized. The results show that when the water content increases from 0.5% to 7%, the maximum erosion rate of the PSS increases first and then decreases, reaching a maximum value of $5.341 \times 10^{-5}$ kg/(m$^2$·s) when the water content is 2%. The maximum erosion rate of MWM is linearly positively correlated with the water content. When the gas production rate increases from 3 to 10 m/s, the maximum erosion wear of defects increases from $5.108 \times 10^{-7}$ to $1.247 \times 10^{-5}$ kg/m$^2$, and the maximum erosion wear of MWM increases from $4.728 \times 10^{-8}$ to $1.743 \times 10^{-6}$ kg/m$^2$. Through orthogonal experimental analysis, it is found that the velocity has a significant effect on the erosion of the PSS. Based on this, the inlet and outlet flow channels of the screen pipe are optimized. The maximum erosion rate of the optimized PSS model is reduced by 25.7%, and the maximum erosion rate of MWM is reduced by 19.7%. The water-bearing gas well should properly control the mining speed at the initial stage of mining, and then increase after the formation of a stable sand bridge, and reduce the concentrated erosion caused by the drag force by optimizing the width of the inlet and outlet of the flow channel, which can effectively improve the service life of the screen pipe of the water-bearing gas well.


## 1. Introduction

As a low-carbon clean energy, natural gas has the characteristics of abundant reserves and is widely used in power generation, chemical industry and other fields (Akash et al., 2024). However, how to produce gas with low cost and high efficiency is an urgent problem to be solved. After a period of time of gas well mining, a large amount of water is produced, which will not only reduce the gas production rate and increase the cost of wastewater treatment, but also cause corrosion and erosion to the production casing and reduce the service life of the production casing. Especially in unconsolidated sandstone gas reservoirs (Li et al., 2023; Liu et al., 2024), the sandstone near the wellbore is easily damaged by strong stress, and the fine sand enters the wellbore with the fluid, resulting in sand production (Dong et al., 2017). Sand production in gas wells will not only cause erosion of production equipment

* Corresponding author.
*E-mail address:* dengfucheng128@163.com (F.-C. Deng).
Peer review under the responsibility of China University of Petroleum (Beijing).

https://doi.org/10.1016/j.petsci.2025.12.021

(Yang et al., 2024; Xie et al., 2025), but also cause excessive sand production and even cause sand burial in production layers or wellbores, which will seriously affect the production of gas wells (Wang et al., 2024; Dou et al., 2025). Therefore, it is of great significance for the long-term safe exploitation of natural gas resources to improve the service life of water-bearing gas well screens.

Erosion wear is one of the main reasons for the failure of sand control screen (Alghurabi et al., 2021; Amadi et al., 2024; Chen et al., 2024; Zambrano et al., 2025). CFD-based erosion modelling is an approach that enables erosion prediction for a variety of conditions (Alghurabi et al., 2021; Ismail et al., 2022; Deng et al., 2024b). Many scholars try to use CFD simulation to explore the influence of various engineering factors on the erosion of screen pipe or establish the erosion model of screen pipe (Zeng et al., 2023; Chi et al., 2024). Procyk (Procyk et al., 2015) proposed an empirical erosion model for MWM based on experimental research and CFD. Zhang et al. (2020) used CFD to simulate the erosion wear of deep-water gas well screen, developed an erosion model, and predicted the life of the screen. Ismail et al. (2022) and Abduljabbar et al. (2024) used four erosion models of CFD to study the effect of different particle size distributions on screen erosion. Previous studies have revealed the local erosion mechanism of the screen and established different erosion models using experimental and numerical simulations. However, these studies are not able to accurately describe the impact of a single particle on the erosion of the screen pipe during the sand escape process.

Corrosion will accelerate the failure of sand control screens in water-bearing gas wells (Safaei et al., 2023; Jing et al., 2024; Sarkar et al., 2023). Domestic oil and gas reservoir development has entered a period of high temperature, high pressure and high water cut. The corrosion environment with high content of $CO_2$, $Cl^-$, $H_2O$ causes internal corrosion of production casing, which causes great harm to oil and gas exploitation (Zhu et al., 2021; Ye et al., 2025). Scholars have successively studied the effect of corrosion on the life of downhole production tools. Mansour et al. (2025) studied the effects of temperature, $Cl^-$ and $CO_2$ partial pressure on the corrosion of N80 casing. Zhou et al. (2024) established a life prediction model considering the attenuation of mechanical properties and the fluctuation of casing stress. The effects of internal pressure and $CO_2/H_2S$ partial pressure on service life are analyzed. However, for sand control screen, corrosion is the main chemical reaction process of failure, and erosion is the main physical process of failure (Wong et al., 2003). It is necessary to combine the two to analyze the failure mechanism of sand control screen (Chen et al., 2022; Fu et al., 2025; Li et al., 2025).

The commonly used calculation models of screen pipe erosion include Discrete Phase Model (DPM) (Constien and Skidmore, 2006; Zhu et al., 2020), Discrete Element Method (Ismail et al., 2022), Dense Discrete Particle Model (Shi et al., 2023; Wang et al., 2023), etc. Considering that the volume fraction of sand is very small. In the process of gas-water carrying sand, sand is mainly affected by gravity and fluid drag, and it is necessary to accurately track the path of a single particle, so the DPM model is selected for simulation.

In this paper, based on the production data of X well in a gas field in western China, the Computational Fluid Dynamics coupled with Discrete Phase Model (CFD-DPM) method and the self-made experimental device are used to study the screen erosion mechanism of water-bearing gas wells. The dynamic mesh layer laying method is used to simulate the downhole corrosion environment. By tracking the trajectory of a single particle (Ding et al., 2021), three sand flow erosion models were established according to the trajectory characteristics, and the effects of different working conditions on the erosion rate of PSS and MWM were discussed. The root causes of the influence of water content and gas production rate on the service life of sand control screen are revealed, and the structure of PSS for water-bearing gas wells is optimized. The optimized new screen structure can reduce the maximum erosion rate of the screen pipe by 26%. By optimizing the scheme of gas production rate, the sand production time of water-bearing gas wells can be further delayed, and the long-term safe development of natural gas can be realized. The research scheme of this paper is shown in Fig. 1.

## 2. Feasibility verification of the model

### 2.1. Erosion experiment of the screen

Considering the low sand content and the need to accurately track the trajectory of particles to study the erosion mechanism, the DPM model is selected for simulation. The DPM model does not consider the particle volume so cannot simulate particle blockage. In the actual erosion process of the MWM, a small sand bridge may be formed at the gap of the mesh, thus forming a local blockage. Therefore, it is necessary to test the error of the DPM model through the erosion test of the MWM. The erosion experiment uses multiple sets of repeated experiments to take the mean. The comparative analysis of erosion experiment and simulation is shown in Fig. 2, including mass loss and erosion morphology.

In this paper, a self-made erosion experimental device was used to simulate the downhole environment for erosion experiments. The experimental device consists of three parts: simulation system, circulation system and erosion system. The main component of the experimental device is a high-pressure kettle (HPK), which is designed as an annulus. The erosion bench divides the space in the HPK into two parts, and the experimental samples are installed on the erosion bench. The connection relationship between each system component and HPK is shown in Fig. 2(a). The parameters used in the test are taken from well X, as shown in Table 1.

The high-pressure pump sends experimental oil into the HPK through the pipeline. Inside the reactor, the experimental oil mixes with the sand samples and flows through the experimental samples, simulating the downhole erosion process. The sand samples, pre-placed at the bottom of the HPK according to the experimental requirements, are sampled and analyzed for particle size distribution. At the bottom of the HPK, four oil inlets are symmetrically arranged, pointing towards the bottom to facilitate sand washing. In the upper part of the HPK, there is an oil inlet facing the experimental sample, used to clean the mud cake from the sample. The MWM sample is welded onto a positioning plate to create the experimental sample, as shown in Fig. 2(c). Before the test, the experimental samples are cleaned and then dried in an oven. The original weight of the samples is recorded. After the test, the same steps are repeated, and the weight of the sample is recorded again.

The test results of the experiment are shown in Table 2. The sample pairs before and after the experiment are shown in Fig. 2(c). After the experiment, there were still a small number of sand samples on the MWM, and there were many bright spots in the middle, indicating that the mass loss in this area is large.

The flow channel model and mesh division of the experimental samples are shown in Fig. 2(b). The boundary conditions, as well as the settings for the inlet and outlet, have been clearly indicated. To control the number of meshes and ensure mesh quality, the MWM was expanded from a circular to a square shape. The total number of tetrahedral meshes exceeded 1.7 million. The interface between the two grids is the internal surface, where the data from the tetrahedral grid is transmitted to the hexahedral grid interface to enable hybrid grid computing.

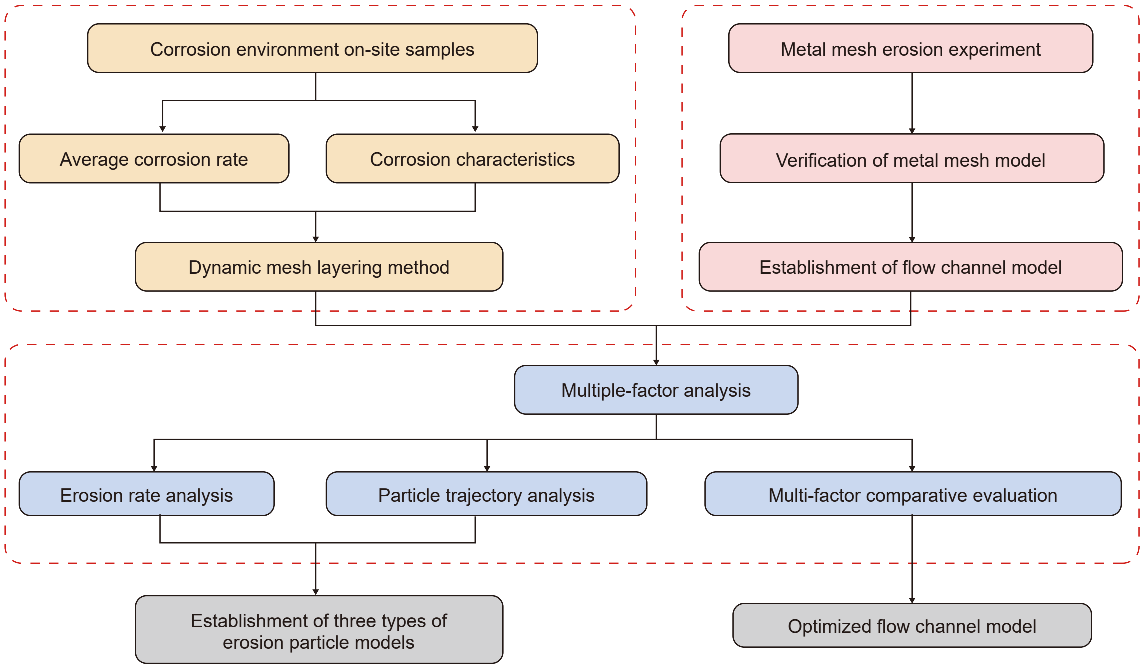


**Fig. 1.** Research scheme of erosion and corrosion mechanism.

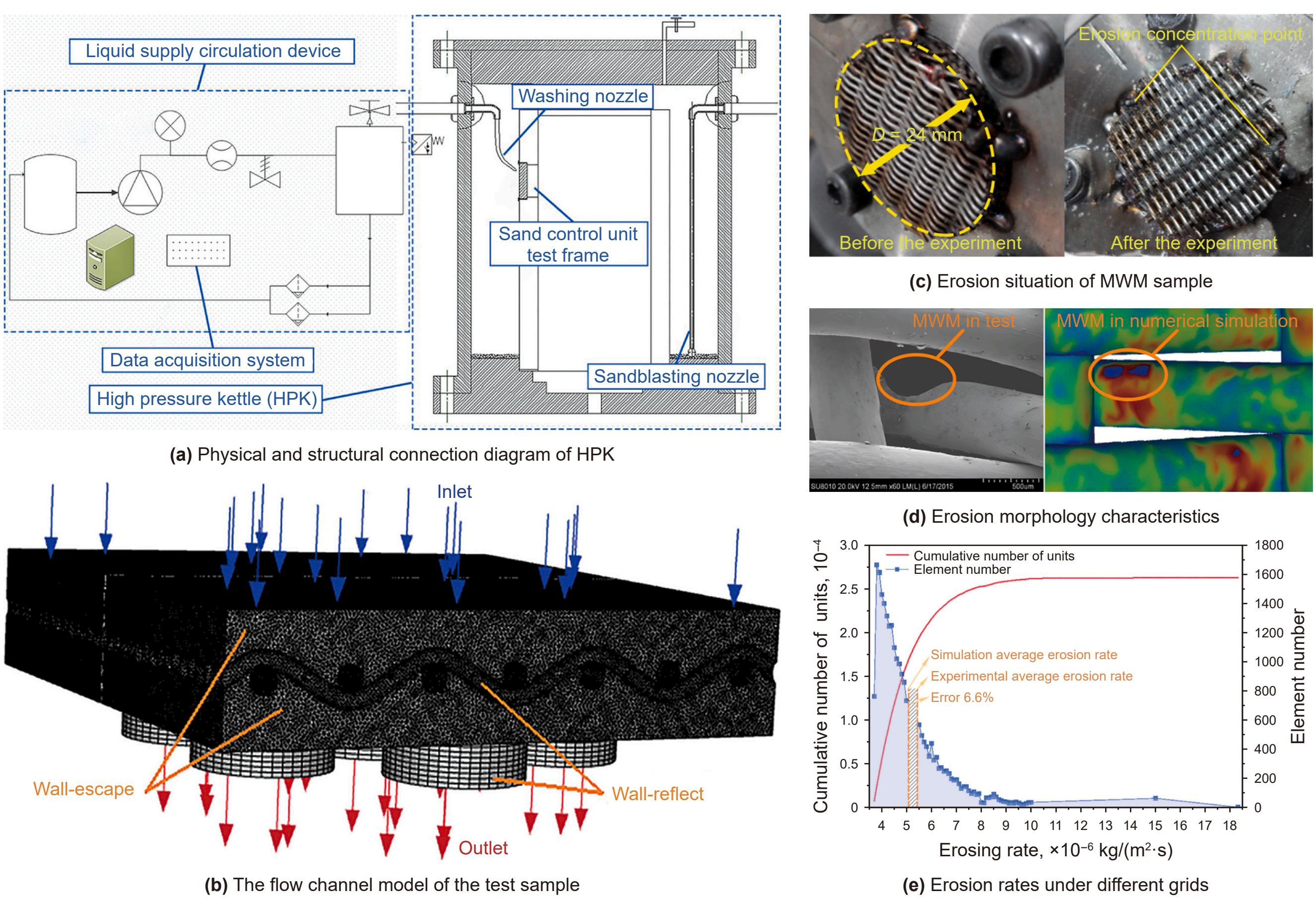


**Fig. 2.** Erosion experiment and simulation of the MWM.

**Table 1**
Data in the process of underground environment simulation test.

| Fluid viscosity, mPa·s | Median size *D*50, μm | sand concentration, % | Screen sand retaining accuracy, μm | Maximum production pressure difference in annulus, MPa |
|---|---|---|---|---|
| 20 | 35 | 3 | 350 | 5 |

**Table 2**
Data in the process of fixed production pressure difference test.

| Production pressure differential, MPa | Erosion time, min | Quality before experiment, g | Quality after the experiment, g | Erosion rate, g/min | Fluid flow rate, kg/min | Fluid flow velocity, m/s |
|---|---|---|---|---|---|---|
| 2 | 787 | 30.734 | 30.568 | $2.109 \times 10^{-4}$ | 14.8 | 2.383 |

The numerical simulation calculates the ideal boundary conditions, with the maximum erosion rate representing the ideal result. However, sand blockage and deformation of the MWM in the experiment cannot be simulated in real time, so the maximum erosion rate cannot be used as a verification index. Instead, the erosion morphology, erosion area, and cumulative mass loss can be compared between the numerical simulation and the experimental results. Fig. 2(d) illustrates the erosion morphology characteristics of the MWM. The experimental results show that erosion occurs on the weft yarn, with the weft yarn beneath the warp yarn experiencing the largest mass loss. The numerical simulation results indicate that erosion is primarily concentrated at the bottom of the "U"-shaped part of the weft. The experimental results align closely with the erosion distribution observed in the numerical simulation, confirming that the DPM model method is feasible.

As shown in Fig. 2(e), according to the numerical simulation results, the average erosion rate of the MWM is $5.112 \times 10^{-6}$ kg/($m^2$·s), and the mass loss of the MWM will be 0.155 g in 787 min (calculated by the sum of mass loss on all grids), which is 6.6% smaller than the experimental mass loss. The error of the numerical simulation results is within a reasonable range, and the DPM model method is feasible.

### 2.2. Corrosion experiment of the screen

The service life of sand control screen in X well is much lower than the design expectation. It is necessary to study the failure mechanism of sand control screen. During the abnormal shut-in period, the X well was overhauled, and sand samples were collected at the wellhead and in the wellbore. Through the component analysis of the produced water, it was found that the $Cl^-$ concentration in the water was abnormal, and the $Cl^-$ concentration was kept above 30.23 g/L. In the produced water, a small amount of $CO_3^{2-}$ and $SO_4^{2-}$ were detected, indicating that the underground environment was highly corrosive.

Acid gases such as $CO_2$ and $H_2S$ have a strong corrosive effect on the sand control screen pipe. When these gases react with water, they become even more corrosive. To investigate this, the downhole environment of X well in a condensate gas field in the Tarim Basin, which contains $CO_2$ and $H_2S$ gases, was simulated, and a corrosion experiment was conducted. Well X is a water-bearing gas well, and the water-gas ratio significantly increased before the shut-in maintenance, as shown in Fig. 3(a). Therefore, it is essential to focus on the impact of water content changes on corrosion.

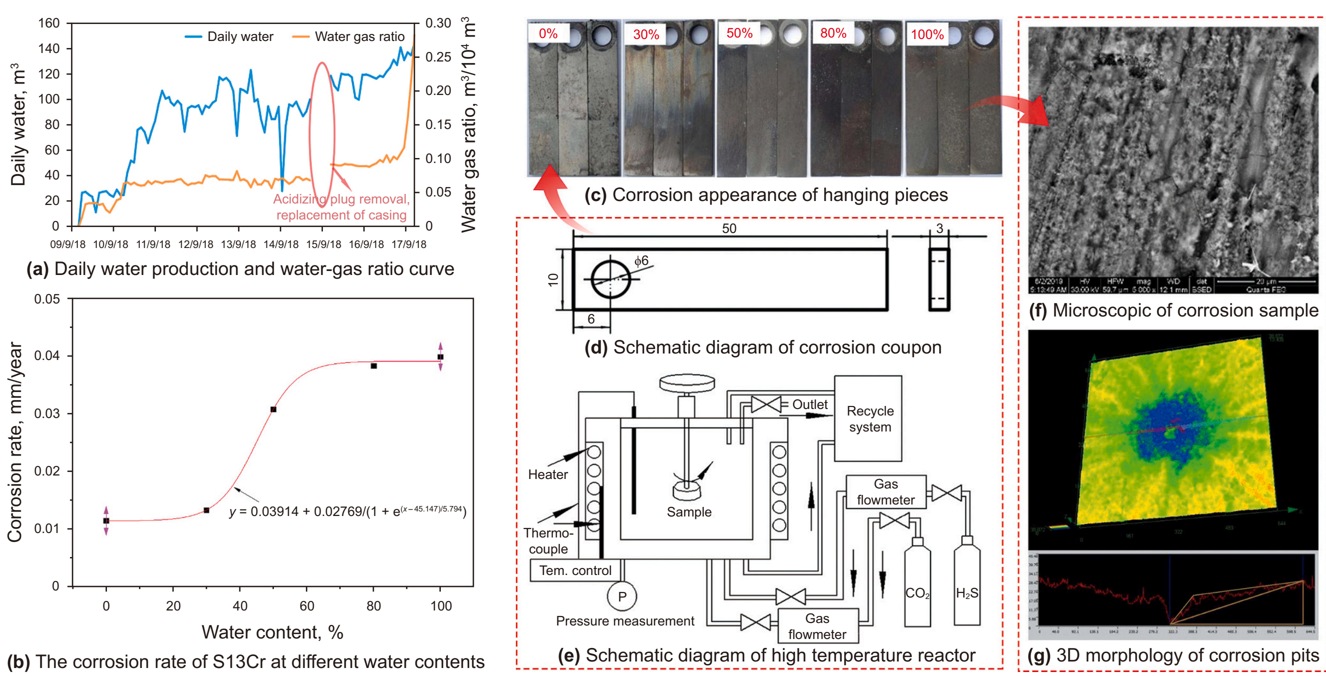


**Fig. 3.** Corrosion experiment of S13Cr under different water content.

Condensate gas can change its state under certain conditions and liquefy into condensate oil. To measure the corrosion rate and defect morphology of the sand control screen under varying water content, a corrosion medium was prepared using a mixture of water and condensate oil in a specific volume ratio. The average corrosion rate of the material was determined using the weight loss method in the corrosion experiment. The material tested for the hanging piece was S13Cr martensitic tubing steel, with its chemical composition shown in Table 3. The raw S13Cr stainless steel materials were processed into hanging pieces, as illustrated in Fig. 3(d).

In this study, the effect of water content on the corrosion of S13Cr stainless steel was investigated. 5 different corrosive media with varying water content were prepared by mixing water and condensate oil according to volume percentage. Other environmental conditions were set based on the results of downhole measurements. The experimental conditions for corrosion are shown in Table 4. Fig. 3(e) presents the schematic diagram of the high-temperature reactor device, where the corrosion reactions were carried out under high temperature and high pressure. During the experiment, the motor drove the clamping device to rotate the hanging piece, simulating the gas flow process.

In the preparation stage of the experiment, the corrosive medium was prepared according to the experimental plan. The metal hanging pieces were degreased and dehydrated, and then their sample size was measured and weighed. In the experimental assembly stage, after the hanging piece was securely fixed, the prepared corrosive medium was added to the HPK according to the experimental requirements. The solution depth was adjusted to ensure that the hanging piece was completely immersed. Finally, the HPK reactor was sealed and installed.

In the experimental stage, $N_2$ was first introduced into the HPK for 2 h to remove $O_2$ from the reactor. After the deoxygenation is completed, the resistance wire was heated to reach the specified temperature in the reactor, and then the $H_2S$ and $CO_2$ gas were injected into the reactor and allowed to stand for 30 min to fully dissolve. The $CO_2$ and $H_2S$ partial pressure were maintained at the set value respectively throughout the experiment. Finally,the motor was started and then maintained a certain speed.

Each experiment lasted for 14 days. At the end of the experiment, the surface corrosion of the hanging piece and the adhesion of the corrosion products were recorded. After the reaction, the hanging piece underwent dehydration treatment, followed by immersion in an acidic cleaning solution for 5 min. The hanging piece was then removed, and the corrosion products were wiped off. The acid was removed by washing with water and other methods. The dehydration and weighing procedures were then repeated. The experimental results were processed using the weight loss method. The average corrosion rate of the coupon was calculated using Eq. (1) for different water contents.

$$V_c = \frac{3650 \times (m_0 - m_t)}{\rho s t} \tag{1}$$

In the formula, $V_c$ is the corrosion rate, mm/year; $\rho$ is the coupon density, g/cm$^3$; $s$ is the surface area of the coupon, cm$^2$; $t$ is the corrosion time, d; $m_0$ is the mass of the coupon before corrosion, g; $m_t$ is the mass of the coupon after corrosion, g.

At different water content, the average corrosion rate of S13Cr is shown in Fig. 3(b). The maximum water-gas ratio recorded by X well is $3.36 \times 10^{-3}$ m$^3$/m$^3$, that is, the water content is 0.336%. According to the fitting curve of the average corrosion rate and water content in Fig. 3(b), when the water content is 0%–20%, the increase of corrosion rate is less than 0.1%. Therefore, it is considered that the corrosion rate of sand control screen in X well is 0.0115 mm/year in the production cycle.

After the corrosion experiment, the corrosion products on the surface of the hanging piece were removed. The appearance of the hanging pieces with different water contents is shown in Fig. 3(c). The hanging pieces exhibited uniform corrosion characteristics, with no particularly prominent pitting.

- When the water content was 0%, the surface of the hanging piece retained its metallic texture, and the traces of mechanical processing were more visible.
- At 30% water content, the lower part of the hanging piece became dark brown, showing significant corrosion, though the traces of mechanical processing were still apparent.
- When the water content exceeded 50%, corrosion products increased, and the corrosion area covered the entire hanging piece, except for the part covered by the nut.
- At 100% water content, the hanging piece was observed under a microscope (Fig. 3(f)). The surface was heavily covered with corrosion products, and many cracks appeared in the corrosion product layer. These cracks exposed the raw material underneath and accelerated the corrosion rate.

The hanging piece with a water content of 100% was taken to find a deeper corrosion point for laser confocal measurement. The 3D morphology of a corrosion pit is shown in Fig. 3(g). The depth of the corrosion pit is 27.644 μm. The shape of the corrosion pit is similar to the funnel. The section is circular, the radius of the funnel nozzle is 40 μm, the height is 19.866 μm, the radius of the funnel body is 177 μm, and the height is 7.778 μm.

## 3. Establishment of the model

### 3.1. Physical model

A MWM model with a nominal aperture of 160 μm was established, and adjusted according to the optimization method of the flow channel model. The physical model is shown in Fig. 4.

In the numerical simulation of corrosion defects, scholars typically model the distribution of corrosion defects as double-point corrosion, with the cross-section of corrosion pits generally being circular or rectangular (Deng et al., 2024a). The corrosion test results indicate that S13Cr stainless steel undergoes uniform corrosion, meaning corrosion defects can develop at any part of

**Table 3**
Chemical constituents of S13Cr.

| Element | C | Si | Mn | Mo | Cr | Ni | Cu | S | P |
|---|---|---|---|---|---|---|---|---|---|
| Content, % | 0.03 | 0.22 | 0.41 | 2.27 | 13.51 | 5.32 | 0.05 | 0.002 | 0.02 |

**Table 4**
Corrosion test conditions.

| Temperature, °C | $CO_2$ partial pressure, MPa | $H_2S$ partial pressure, kPa | Corrosion medium | Experimental time, d | Material |
|---|---|---|---|---|---|
| 180 | 5.81 | 1.69 | 100% water; 80% water +20% condensate oil; 50% water +50% condensate oil; 30% water +70% condensate oil; 100% condensate oil | 14 | S13Cr |

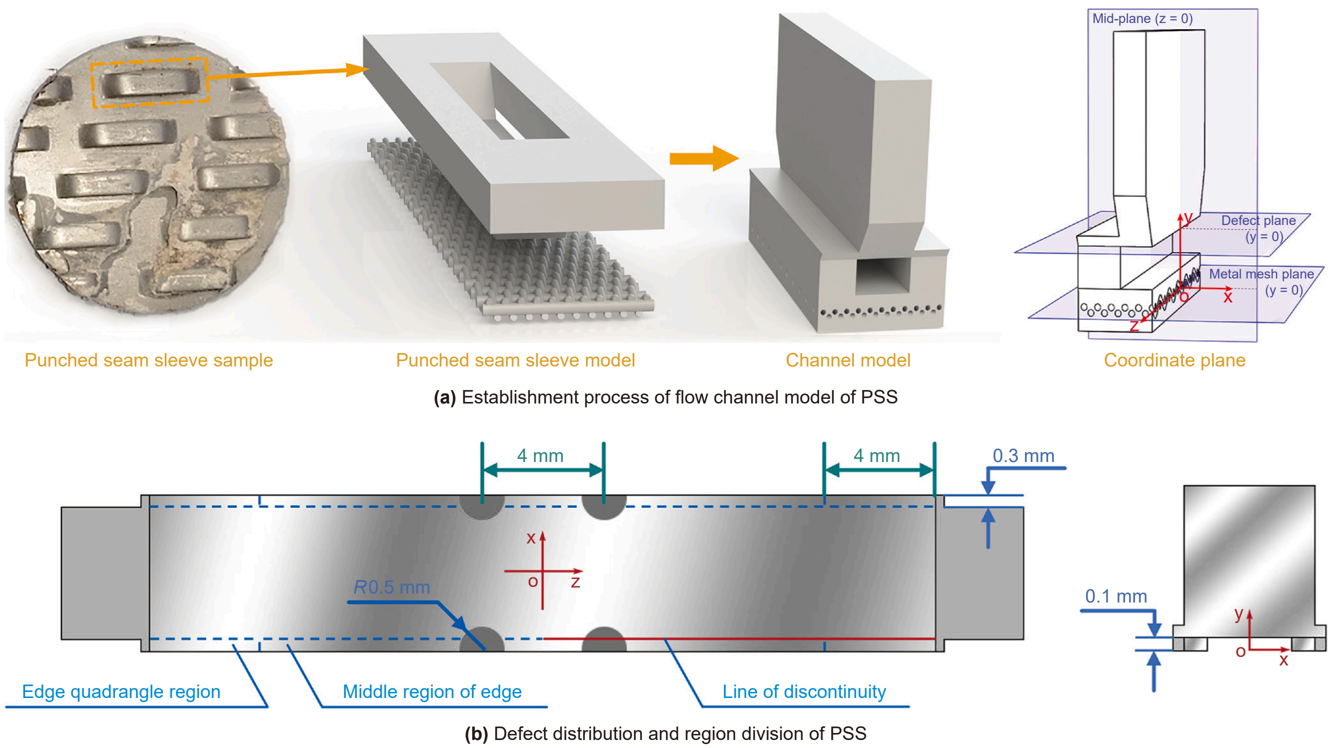


**Fig. 4.** The process and details of PSS physical model establishment.

the screen pipe. The numerical simulation reveals that the most vulnerable area of the PSS is the edge of the bottom surface. In areas with higher erosion rates, the corrosion rate is greater, leading to a faster growth rate of defects. Additionally, these defects alter the boundary of the basin, creating a positive feedback loop that accelerates erosion and significantly shortens the service life of the screen pipe.

Therefore, the defect is set at the bottom of the edge area. Since the cross section of the corrosion pit is circular, the cross section of the corrosion defect is set to a circular or semi-circular radius of 0.5 mm. The discontinuity line in Fig. 4(b) is to read the position of the erosion wear amount. In this paper, the bottom surface of the PSS is divided into three regions, the middle region, the edge middle region and the edge four corner region, which is convenient to describe the erosion distribution area below.

### 3.2. Numerical model

#### 3.2.1. Particle trajectory tracking

In the Lagrangian coordinate system, the motion equation of the particles is integrated to obtain the motion trajectory of the particles. The Euler-Lagrangian method is used to describe the particle motion. The particles are assumed to be mass points, ignoring the interaction between particles, the particles will not break, and the small deformation of the wall is not considered. Under these assumptions, according to Newton's second law, the motion control equation of solid particles per unit mass is obtained by integral operation as follows (Bozzini et al., 2003; Parsi et al., 2014):

$$\frac{\mathrm{d}v_t}{\mathrm{d}t} = F_\mathrm{D} + F_\mathrm{P} + F_\mathrm{other} \tag{2}$$

In the formula, $F_\mathrm{D}$ and $F_\mathrm{P}$ are the drag force and pressure gradient force per unit mass of particles, N/kg, respectively; $F_\mathrm{other}$ is the other force per unit mass of particles, N/kg. Drag force is the most important force on solid particles. The form is as follows (Dickenson and Sansalone, 2009):

$$F_\mathrm{D} = \frac{18\mu}{\rho_\mathrm{p} d_\mathrm{p}^2}\frac{C_\mathrm{d} Re_\mathrm{ep}}{24}(v_\mathrm{a} - v_\mathrm{p}) \tag{3}$$

In the formula, $v_\mathrm{p}$ is the particle velocity, m/s; $v_\mathrm{a}$ is fluid velocity, m/s; $\mu$ is the hydrodynamic viscosity, Pa·s; $\rho_\mathrm{p}$ is particle density, kg/m$^3$; $d_\mathrm{p}$ is the particle diameter, m; $Re_\mathrm{ep}$ is the relative Reynolds number (Morsi and Alexander, 1972):

$$Re_\mathrm{ep} = \frac{\rho_\mathrm{a} d_\mathrm{p} |v_\mathrm{p} - v_\mathrm{a}|}{\mu} \tag{4}$$

$C_\mathrm{d}$ is the drag coefficient (Haider, 1989):

$$C_\mathrm{d} = a_1 + \frac{a_2}{Re_\mathrm{ep}} + \frac{a_3}{Re_\mathrm{ep}} \tag{5}$$

In the formula, $a_1$, $a_2$, $a_3$ are constants, and their values change with the Reynolds number (Morsi and Alexander, 1972). If there is a pressure gradient in the flow field where the particles are located, the particles will be subjected to a force caused by the pressure gradient. The pressure gradient force per unit mass of particles is as follows:

$$F_P = \left(\frac{\rho}{\rho_\mathrm{p}}\right)\nabla p \tag{6}$$

After the solid particles collide with the wall, the velocity of the solid particles decreases, and its kinetic energy decreases. The particle-wall collision rebound model is used to define the recovery coefficient, and the recovery coefficients $e_n$ and $e_t$ are used to measure the energy loss. According to the particle-wall collision rebound model, the change of velocity and energy after the collision of particles with the wall surface is solved (Finnie and McFadden, 1978). For carbon steel, the values of $e_n$ and $e_t$ are:

$$\begin{cases} e_n = 0.993 - 0.0307\alpha + 0.000475\alpha^2 - 0.00000261\alpha^3 \\ e_t = 0.988 - 0.029\alpha + 0.000643\alpha^2 - 0.00000356\alpha^3 \end{cases} \quad (7)$$

#### 3.2.2. Erosion rate model

There are four commonly used erosion rate models, Finnie et al. (1992), McLaury et al. (1997), Oka et al. (1993) and Haugen et al. (1995), which are suitable for the prediction of erosion rate of various materials (Abduljabbar et al., 2021). The material of the PSS is carbon steel, and the standard erosion model can be used (Finnie et al., 1992). The expression is as follows:

$$R_{\text{erosion}} = \sum_{n=1}^{N_{\text{particles}}} \frac{m_{\text{p}} C(d_{\text{p}}) f(\theta) v_{\text{p}}^{b(v)}}{A_{\text{face}}} \quad (8)$$

where, $R_{\text{erosion}}$ is the erosion wear rate of material surface, kg/(m$^2$·s); $N_{\text{particles}}$ is the number of particles colliding with the wall; $m_{\text{p}}$ is the particle mass flow rate, kg/s; $C(d_{\text{p}})$ is the function of particle diameter, and the fixed value is $1.8 \times 10^{-9}$; $\theta$ is the impact angle between the particle and the wall, rad; $v_{\text{p}}$ is the velocity of particles impacting on the material surface, m/s; $b(v)$ is the velocity function of the particle relative to the wall surface, and the fixed value is 2.6; $A_{\text{face}}$ is the area of erosion calculation unit, m$^2$; $f(\theta)$ is the impact angle function of the particle and the wall, and the piecewise polynomial function is used to fit the impact angle function. The impact angle function of the collision between particles and carbon steel is shown in Table 5 (Edwards et al., 2000).

### 3.3. Simulation procedure

#### 3.3.1. Computational parameter

The simulation process includes gas-liquid-solid three phases, namely methane, water, and sand. Their parameters such as velocity and flow rate are shown in Table 6. The particle diameter is 0.05 mm, the particle mass flow rate is 0.01 kg/s, the injection velocity is set to 3 m/s, the inlet velocity of liquid water and methane is 3 m/s, the volume fraction of particles is 3.52%, and the volume percentage of methane is set to 0.995.

According to the corrosion characteristics and rate of the corrosion sample (Deng et al., 2024a), the relevant parameters for the dynamic mesh are extracted, as shown in Table 7. The average corrosion rate is 0.0115 mm/year, so the dynamic mesh rate of controlling corrosion defects is $3.65 \times 10^{-10}$ mm/s. The bottom surface of the defect is set as the moving surface, and the attribute is rigid body. The grid height at the defect is 0.05 mm. Adhering to the principle of grid consistency, the reference grid height is set to 0.05 mm, the collapse factor is 0.3, and the splitting factor is 0.4.

#### 3.3.2. Turbulent flow model

The standard k-ε model has good adaptability in high Reynolds number flow. By comparing with the experimental results, it is found that the model can provide results consistent with the actual flow field. Therefore, the standard k-ε model is selected in this study.

**Table 5**
Impact angle function.

| Serial number | $\theta$ | $f(\theta)$ |
|---|---|---|
| 1 | 0 | 0 |
| 2 | 20 | 0.8 |
| 3 | 30 | 1 |
| 4 | 45 | 0.5 |
| 5 | 90 | 0.4 |

**Table 6**
Detailed erosion parameter.

| Item | Value | Unit |
|---|---|---|
| Methane density | 103.5 | kg/m$^3$ |
| Dynamic viscosity of methane | 0.018 | mPa·s |
| Injection velocity | 3 | m/s |
| Flow rate | 0.01 | kg/s |
| Particle diameter | 50 | μm |
| UC | 1.5 | – |
| Inlet velocity | 3 | m/s |
| Volume percentage of methane | 99.5 | % |

#### 3.3.3. Boundary conditions

Water-liquid and methane are added to the material-continuum phase, with the first phase set as liquid water and the second phase as methane. The gas phase flow field is governed by the non-slip boundary condition, while the wall grid area uses the standard wall function method. The inlet surface is defined as the velocity inlet, with the volume fraction set for the second phase, and the outlet surface is set as a free outflow boundary.

In the channel model of the screen pipe, the wall surface generated by the PSS and the MWM adopts the reflection condition, while the other surfaces adopt the escape condition, as shown in Fig. 5(a). The inlet surface is defined as the injection source for the particles, with the initial velocity of the particles matching the inlet velocity of the fluid. It is assumed that the mass of the particles remains unchanged, and there is no heat transfer. Only the particle density and mass flow rate are specified. The particles are assumed to be uniformly spherical, with sand added as the material-solid phase.

### 3.4. Grid independence verification

An unstructured hexahedral mesh is used to mesh the flow channel of the PSS, with local refinement applied to the defects. The flow channel of the MWM is an irregular model, which is meshed using tetrahedral elements. 6 different mesh configurations for the PSS channels are used in the numerical simulation. Based on the production conditions of X well, the liquid phase in the well is primarily water, and the injection source is defined as the fluid inlet surface.

The maximum erosion rate results for different grid sizes are shown in Fig. 5(b). When the number of grids exceeds 150,000, the maximum erosion rate changes by no more than 5%. Increasing the number of grids further does not result in significantly higher calculation accuracy. Therefore, the fourth grid configuration is chosen for subsequent calculations. The results of the fourth grid configuration are shown in Fig. 5(a), with the boundary conditions and inlet/outlet settings clearly marked in the figure.

**Table 7**
Detailed corrosion parameter.

| Item | Value | Unit |
|---|---|---|
| Average corrosion rate | 0.0115 | mm/year |
| Corrosion defects | $3.65 \times 10^{-10}$ | mm/s |
| Grid height at the defect | 0.05 | mm |
| Collapse factor | 0.3 | – |
| Splitting factor | 0.4 | – |

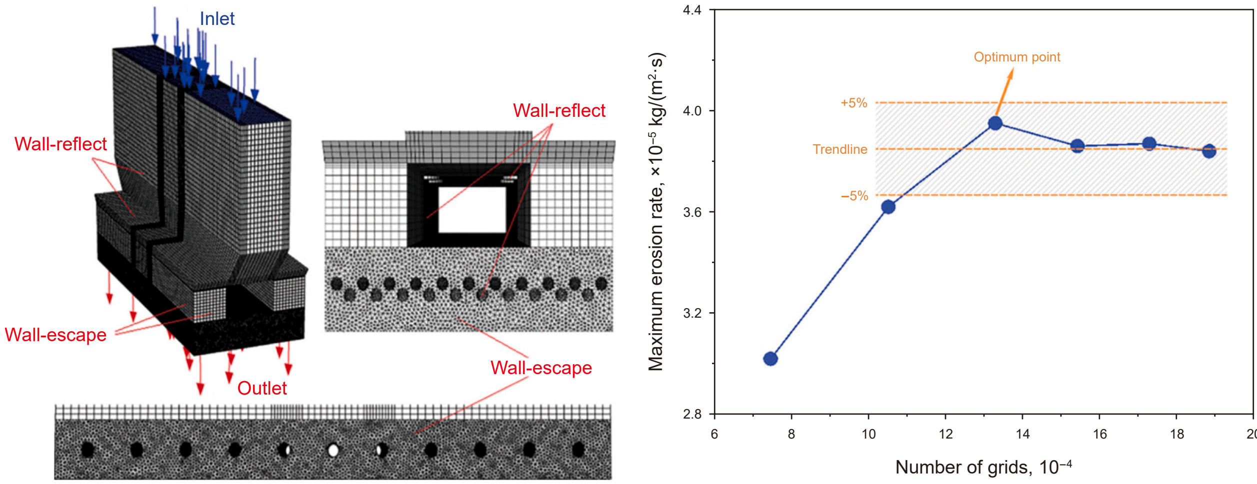


**(a)** The meshing results of the flow channel model of the PSS **(b)** Grid independence analysis results

**Fig. 5.** Meshing and independence verification of the PSS.

## 4. Result and discussion

### 4.1. The influence of corrosion

In this paper, the layering method is used to control the deformation of the defect, ensuring that the defect surface moves unidirectionally at a constant speed. Based on the corrosion test results, the average corrosion rate of S13Cr stainless steel was determined to be 0.0115 mm/year, and the dynamic mesh rate was set to $3.65 \times 10^{-10}$ mm/s. From the perspective of the model boundary, the defect depth changes over time, and the dynamic mesh rate is set to 0 mm/s to compare the effect of corrosion on the erosion behavior. Fig. 6 shows the maximum erosion wear of the PSS and MWM when the dynamic mesh rate is 0 mm/s.

The velocity and impact angle of all particles are counted, as shown in Fig. 7. It is found that the particle velocity is distributed in two intervals of 0.7–1.8 m/s and 2.7–3.7 m/s, corresponding to the impact angle distribution of 15°–55° and 75°–90°. When the dynamic mesh rate is 0 and $3.65 \times 10^{-10}$ mm/s, the average velocity of particles is 2.991 and 3.002 m/s, respectively, and the average velocity increases by 0.37%. When the dynamic mesh rate is 0 and $3.65 \times 10^{-10}$ mm/s, the cumulative number of nodes is 870, and the cumulative erosion wear is $1.323 \times 10^{-4}$ and $1.333 \times 10^{-4}$ kg/m$^2$, respectively. This shows that the corrosion increases the velocity and impact angle function values, and slightly reduces the number of particles, resulting in an increase in the cumulative erosion wear at the defect of PSS.

### 4.2. The influence of water content on erosion law

With the exploitation of gas wells, the natural gas reserves in the formation are gradually reduced, and the water content will increase significantly while maintaining a certain amount of production. The water content has a certain influence on the erosion law of the sand control screen, and the water content is set to 0.5%, 1%, 2%, 3%, 5% and 7%, respectively. At different water content, the maximum erosion wear amount of the defect is shown in Fig. 8(a). When the water content is from 0.5% to 7%, the maximum erosion wear amount of the defect increases first and then decreases. The maximum erosion area (red) gradually changes from point distribution to linear distribution, and the area of the main erosion area (cyan) decreases obviously and moves to the edge. The position and size of the maximum erosion wear zone of MWM at different water contents are shown in Fig. 8(b). When the water content is from 0.5% to 7%, the maximum erosion wear of MWM continues to increase, the area of the maximum erosion wear area

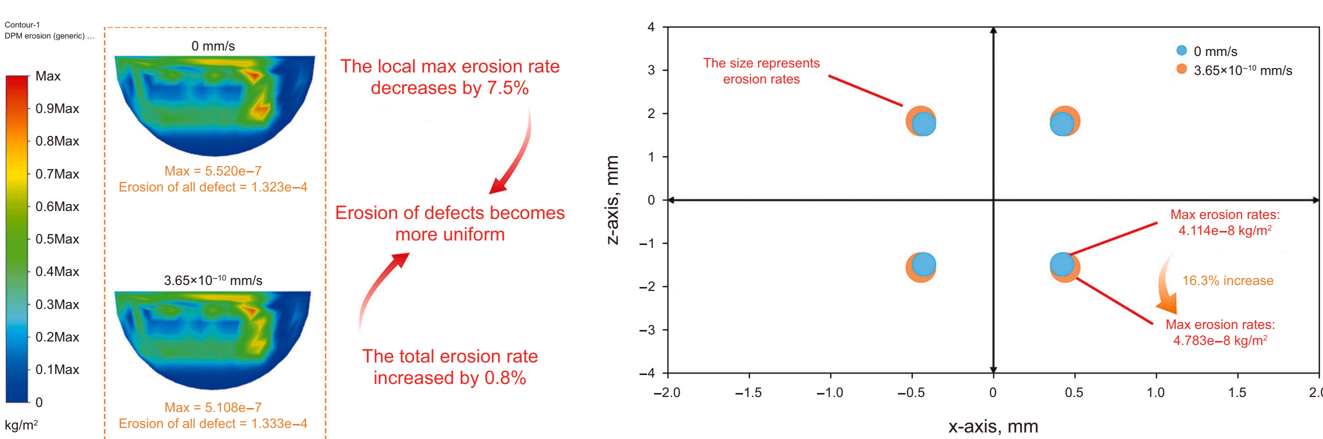


**(a)** The errosion rate of defects of PSS under different dynamic mesh **(b)** The position and erosion rate of MWM under different dynamic mesh

**Fig. 6.** Comparison of dynamic mesh and non-dynamic mesh of the PSS and MWM.

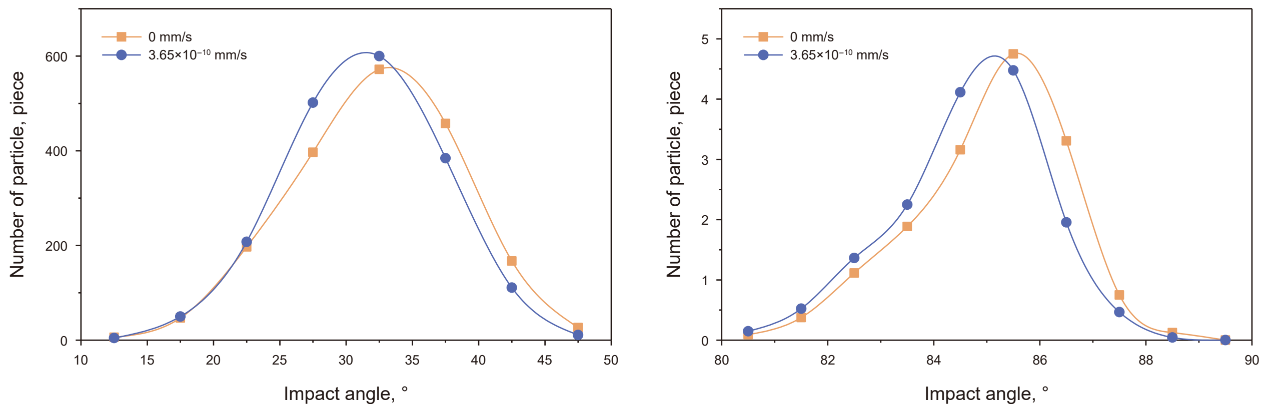


**Fig. 7.** The relationship between the number of particles and the impact angle.

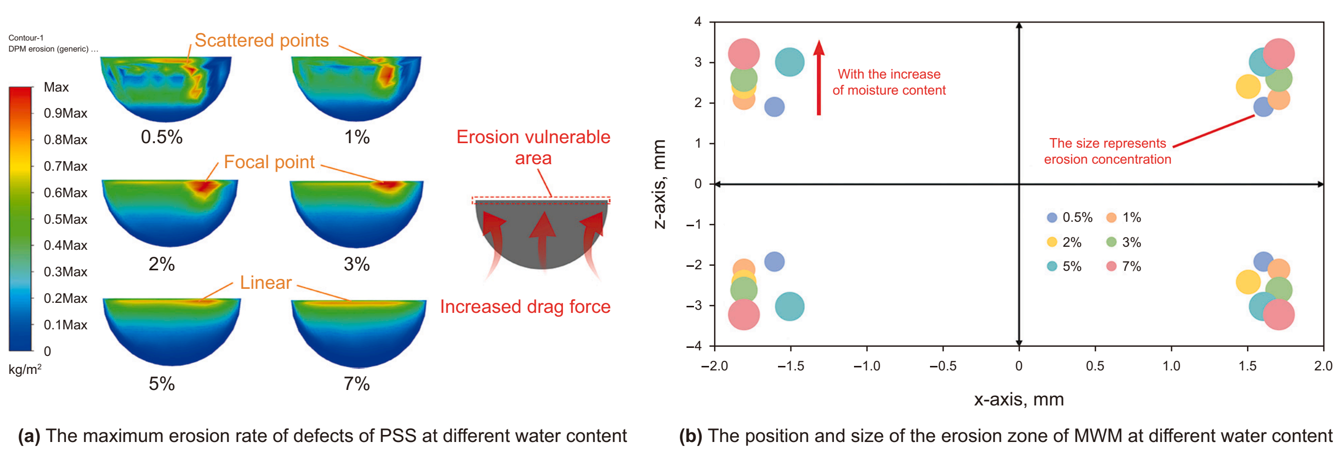


**Fig. 8.** The maximum erosion rate of PSS and MWM at different water content.

continues to expand, and the displacement of the erosion area along the x-axis is increasing. It can be seen from the drag force Eq. (3) that the drag force is related to the fluid viscosity. The dynamic viscosity of water is two orders of magnitude larger than that of methane. The larger the water content, the greater the drag force on the particles, and the greater the displacement along the x-axis.

Fig. 9 is the position distribution map of particles when the water content is 0.5%. Between the PSS and the MWM, the particles are obviously divided into two parts. One part of the particles directly rushes to the MWM, and the other part of the particles escapes from the side of the x-axis direction and rushes to the MWM outside the model. These two parts of particles have their own characteristics. The former has a small number, but the velocity is large, and the erosion area is more concentrated. The latter has a large number, but after multiple erosions on the wall surface, the velocity after the rebound is greatly reduced, and the

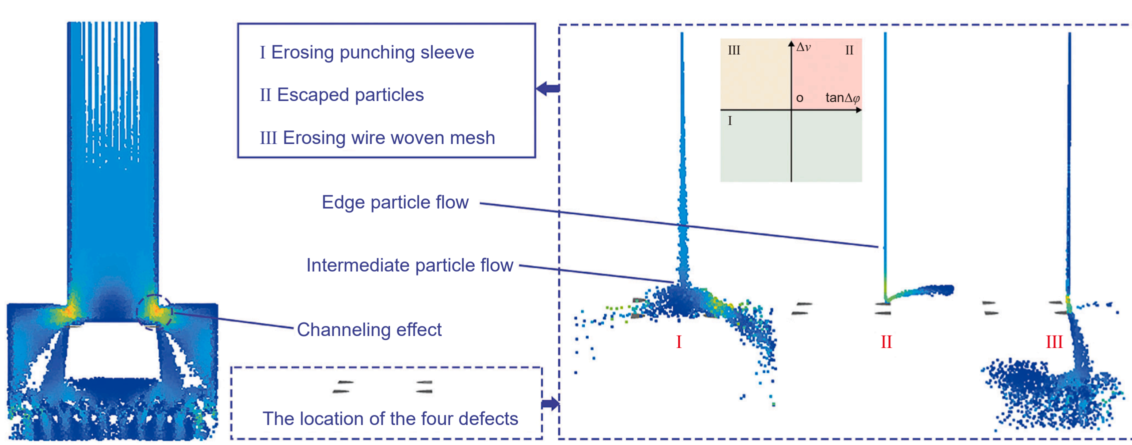


**Fig. 9.** The distribution of particles on the mid plane at different water content.

erosion area is very wide. According to the erosion model Eq. (8) and the numerical simulation results, the former is the main reason for the damage of the MWM. In order to confirm the trajectory of the particles, only the position of a single particle flow is viewed. According to the trajectory of these particle flows, it can be divided into three categories.

- Type I particles are injected from the middle area, and the velocity decreases greatly after hitting the bottom of the PSS. Under the action of drag force, it escapes from the side of the x-axis direction;
- Type II particles are injected from the area directly opposite to the defect. After hitting the bottom of the defect, there is a significant rebound, which is obviously affected by the drag force, and the motion trajectory is relatively concentrated, escaping from the side of the x-axis direction;
- Type III particles are injected from the vicinity of the wall on both sides, and directly impact the MWM through the double-slit outlet under the action of drag force. The most serious erosion for MWM is type III particles.

Due to the complex structure of MWM, the data of directly processing type III particles is more complex, and type III particles will erode MWM many times. Therefore, this paper uses indirect method to study the influence of water content on type III particles.

Through the velocity vector and its change, the three types of particles are divided more accurately in mathematical form:

$$\begin{cases} \text{I}: \Delta\nu < 0 \\ \text{II}: \Delta\nu > 0, \tan\Delta\varphi > 0 \\ \text{III}: \Delta\nu > 0, \tan\Delta\varphi < 0 \end{cases} \tag{9}$$

In the formular, $\Delta\nu$, The velocity increment when the particles enter the PSS to first collision; $\Delta\varphi$, The change angle of velocity vector after the first collision of the PSS.

At different water content, the position distribution of the same particle flow is shown in Fig. 10. It can be seen from Fig. 10 that the emergence angle $\alpha$ and the erosion angle $\theta$ are complementary, that is $\alpha + \theta = 90°$. When the water content is 0.5%–7%, the number of particles in the flow channel model gradually decreases. At the same time, the emergence angle $\alpha$ becomes larger, and the displacement of particles along the x-axis direction becomes larger. This shows that the greater the water content, the greater the drag force on the particles, and the greater the particle velocity. At the same time, it can be seen that the larger the water content, the smaller the angle of particle erosion MWM, the larger the impact angle function value, and the greater the erosion rate. The maximum dynamic erosion rate of MWM is linearly positively correlated with water content. Within the scope of this study, the maximum dynamic erosion rate of the PSS is greater than the maximum dynamic erosion rate of the MWM. When the water content exceeds a certain value, the maximum dynamic erosion rate of the MWM may be greater than the maximum dynamic erosion rate of the PSS, which requires further research.

The number of particles and the average velocity of erosion defects at different water content are shown in Fig. 11. When the water content is 0.5%–7%, the number of particles with erosion defects gradually decreases, and the average rate increases significantly. Because the number of type I particles is fixed and escapes directly from the side, the erosion rate of MWM is not affected. With the increase of water content, the drag force of particles increases greatly, and some type II particles are transformed into type III particles, which directly erodes MWM. The increase of particle number is one of the reasons for the increase of maximum dynamic erosion rate of MWM. Moreover, it can be seen from Figs. 10 and 11 that the average velocity of type III particles increases with water content, which is one of the reasons for the increase of the maximum dynamic erosion rate of MWM.

### 4.3. Effect of velocity on erosion law

After the water-bearing gas well is mined for a period of time, the sand control screen is gradually blocked by sand, and the permeability is greatly reduced. After the implementation of plugging removal measures, the permeability of sand control screen will be restored to a certain level. The permeability of sand control screen reflects the flow rate of gas well mining, and the inlet flow velocity are set to be 3, 4, 5, 6, 8 and 10 m/s, respectively. The flow velocity here is the gas velocity flowing into the PSS. It is calculated according to the production rate of the gas well. The specific formula is as follows:

$$v = \frac{n}{3600 \times 24 \times (\pi d L \Phi)} \tag{10}$$

In the formula: $v$ is the flow velocity of the gas through the PSS, m/s; $n$ is the daily gas production rate, $m^3/d$; $\Phi$ is the PSS opening rate; $d$ is the diameter of the sand control screen in the production section, m; $L$ is the length of gas production section, m.

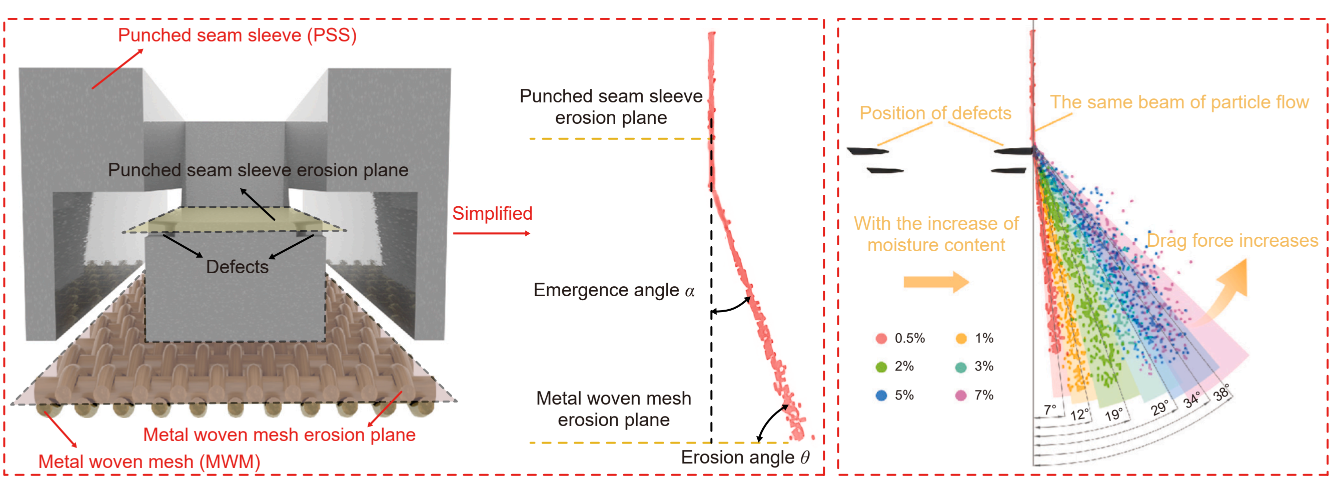


**Fig. 10.** The distribution of the same particle flow at different water content.

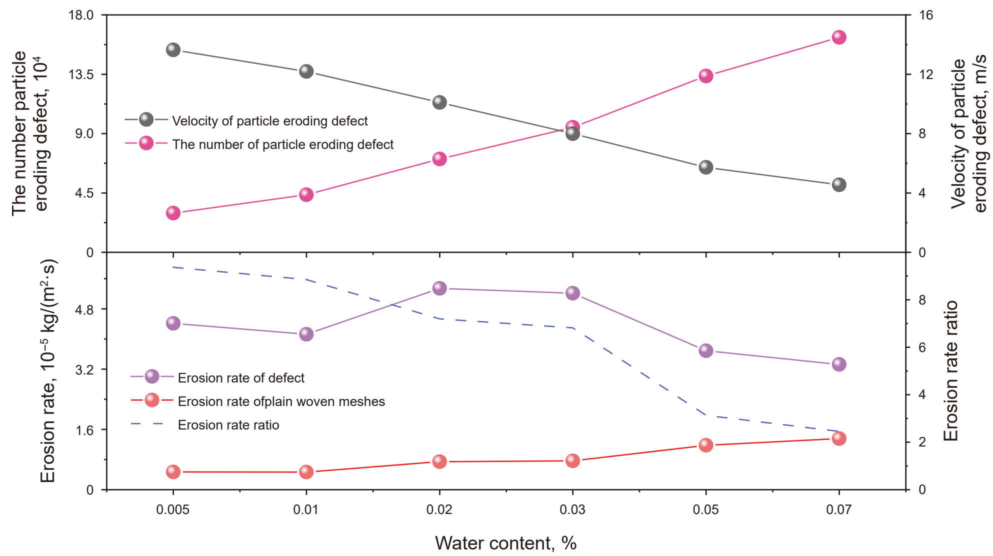


**Fig. 11.** Particle velocity and number at the defects of PSS (above) and the maximum dynamic erosion rate at different water content (below).

At different velocity, the maximum erosion wear of the defect is shown in Fig. 12(a). When the velocity increases from 3 to 10 m/s, the maximum erosion wear of the defect increases from $5.108 \times 10^{-7}$ to $1.247 \times 10^{-5}$ kg/m$^2$. The distribution area of the maximum erosion wear amount of the defect presents an "L" shape, and the width of the "L" increases with the velocity. Fig. 12(b) shows the position distribution of the same particle flow at different velocities. The impact angle of type III particles has no change, so the impact angle function value remains unchanged. The particle flow at this place is mainly type III particles, and a very small part is type II particles. This distribution feature is not affected by velocity changes. Therefore, the maximum erosion wear of MWM increases from $4.728 \times 10^{-8}$ to $1.743 \times 10^{-6}$ kg/m$^2$, but the location and area of the maximum erosion area are almost unchanged. Finally, it can be found that with the increase of velocity, the number of type III particles decreases significantly, and the ratio of defect to the maximum dynamic erosion rate of MWM decreases instead, indicating that the velocity of type III particles relative to MWM should increase significantly.

From Fig. 13, it can be seen that with the increase of velocity, the maximum dynamic erosion rate ratio of defect and MWM becomes smaller and smaller, which indicates that the type of particles is still affected by the change of velocity. With the increase of velocity, the number of particles of erosion defects gradually increases, but the number of particles cannot exceed the total number of particles injected in this section. The maximum number of particles in the erosion defect is 157, 000, that is, the maximum number of particles in each erosion defect is 393 (the number of inlet grids in the defect section is 540). When the velocity increases from 3 to 10 m/s, the number of type I particles is 1877, 2003, 2081, 2279, 2431 and 2680, respectively. Comparing the change of the total number of particles, it shows that some type III particles are converted into type II particles.

### 4.4. Analysis of orthogonal experimental results

Sections 4.2 and 4.3 reveal the influence of water content and gas production rate on sand screen erosion. However, the main factors affecting the erosion of the PSS also include particle diameter and mass flow rate. Therefore, the orthogonal experimental analysis method is used to analyze the multi-factor erosion of the PSS in the water-bearing gas well.

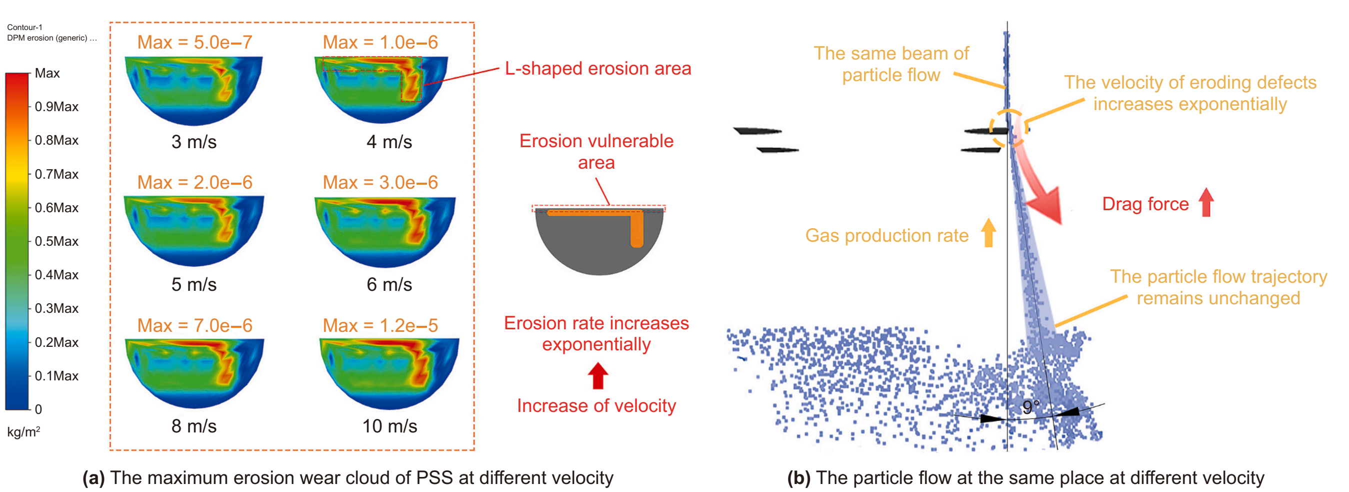


**Fig. 12.** Erosion wear of PSS and MWM at different velocity.

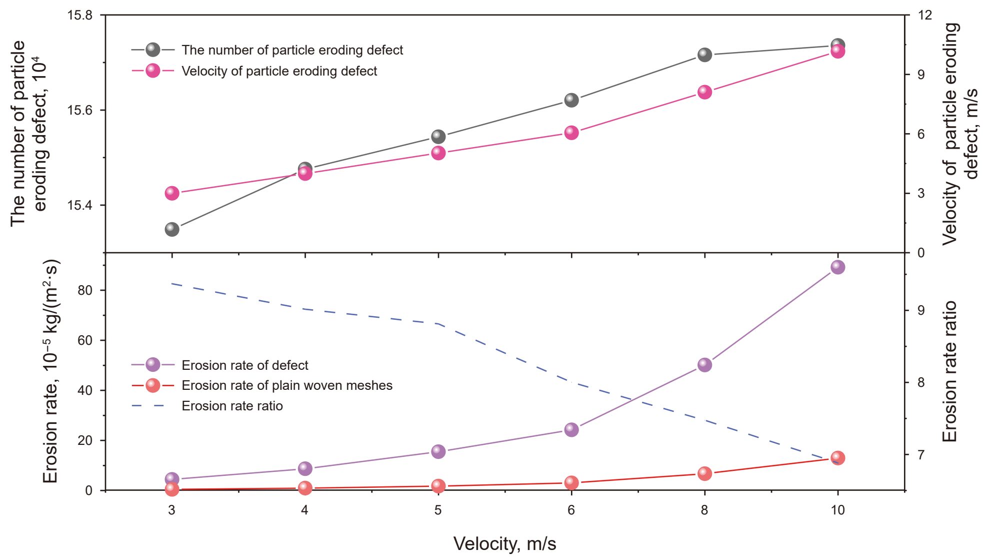


**Fig. 13.** Particle velocity and number at the defects of PSS (above) and the maximum dynamic erosion rate of defects and MWM at different velocity (below).

#### 4.4.1. Numerical simulation results of orthogonal experiment

The level of each factor in Table 8 is substituted into the orthogonal experiment table $L_{16}$ ($5^4$), and the numerical simulation is carried out by using the flow channel model of the PSS with defects. Then, the maximum dynamic erosion rate of the PSS and MWM is collected, and the results are shown in Table 9.

#### 4.4.2. Analysis of orthogonal experimental results

In practical application, we hope that the maximum dynamic erosion rate of the PSS is as small as possible. In order to quickly find out the influence degree of each factor on the maximum dynamic erosion rate, range and variance analysis is needed and gray correlation analysis method is also introduced for auxiliary analysis. Different from the general orthogonal experimental analysis, this range analysis only needs to arrange the order of each factor, and does not need to select the optimal combination. The analysis results are shown in Figs. 14 and 15.

Both variance and gray correlation analysis point to the same result. For both the PSS and MWM, the velocity (factor B) has the greatest influence on the maximum dynamic erosion rate, and the velocity also has a significant effect on the maximum dynamic erosion rate of the PSS. Therefore, controlling the mining speed of water-bearing gas wells can greatly reduce the erosion wear speed. After the sand control screen is in service for a period of time, the sand particles are blocked by the MWM, and the sand bridge is formed in the PSS. The stable sand bridge can act as the sand control medium. After the sand bridge is formed, the mining speed can be appropriately increased. The influence of water content (factor A) on the maximum dynamic erosion rate of MWM is the second. The increase of water content not only reduces the service life of sand control screen, but also greatly increases the mining cost. It is necessary to study the relevant water control technology.

**Table 8**
Factors and levels of orthogonal test table.

| Factor | Level | | | |
|---|---|---|---|---|
| | 1 | 2 | 3 | 4 |
| Water content (A) | 0.5 | 2 | 3 | 5 |
| Velocity (B) | 3 | 4 | 5 | 6 |
| Particle diameter (C) | 0.05 | 0.06 | 0.08 | 0.10 |
| Mass flow rate (D) | 0.002 | 0.006 | 0.010 | 0.015 |

**Table 9**
Numerical simulation results of orthogonal experiment.

| Experimental number | A | B | C | D | Error column | Maximum dynamic erosion rate, $10^{-5}$ kg/($m^2$·s) | |
|---|---|---|---|---|---|---|---|
| | | | | | | PSS | MWM |
| 1 | 1 | 1 | 1 | 1 | 1 | 0.942 | 0.093 |
| 2 | 1 | 2 | 2 | 2 | 2 | 2.865 | 0.352 |
| 3 | 1 | 3 | 3 | 3 | 3 | 5.54 | 0.872 |
| 4 | 1 | 4 | 4 | 4 | 4 | 13.197 | 1.536 |
| 5 | 2 | 1 | 2 | 3 | 4 | 2.307 | 0.519 |
| 6 | 2 | 2 | 1 | 4 | 3 | 7.311 | 1.74 |
| 7 | 2 | 3 | 4 | 1 | 2 | 1.637 | 0.286 |
| 8 | 2 | 4 | 3 | 2 | 1 | 7.608 | 2.299 |
| 9 | 3 | 1 | 3 | 4 | 2 | 2.608 | 0.866 |
| 10 | 3 | 2 | 4 | 3 | 1 | 4.637 | 0.98 |
| 11 | 3 | 3 | 1 | 2 | 4 | 7.739 | 2.03 |
| 12 | 3 | 4 | 2 | 1 | 3 | 4.672 | 0.908 |
| 13 | 4 | 1 | 4 | 2 | 3 | 1.387 | 0.484 |
| 14 | 4 | 2 | 3 | 1 | 4 | 1.752 | 0.381 |
| 15 | 4 | 3 | 2 | 4 | 1 | 18.199 | 3.745 |
| 16 | 4 | 4 | 1 | 3 | 2 | 19.495 | 6.185 |

### 4.5. PSS structure optimization and numerical simulation results

#### 4.5.1. Structure optimization of PSS

Through orthogonal experimental analysis, it is observed that reducing the particle velocity should be the primary focus for optimizing the structure of the sand control screen. Near the double-slit outlet of the PSS, the velocity of the continuous phase increases significantly. At this point, the particles experience the maximum drag force, which does positive work on the particles. This increases the velocity of type II particles, thereby raising the erosion rate of the PSS, and also increases the number of type III particles, which raises the erosion rate of the MWM. By optimizing the structure of the PSS to reduce the velocity of the continuous phase near the double-slit outlet, the drag force can be minimized, thereby reducing the erosion rates of both the PSS and the MWM.

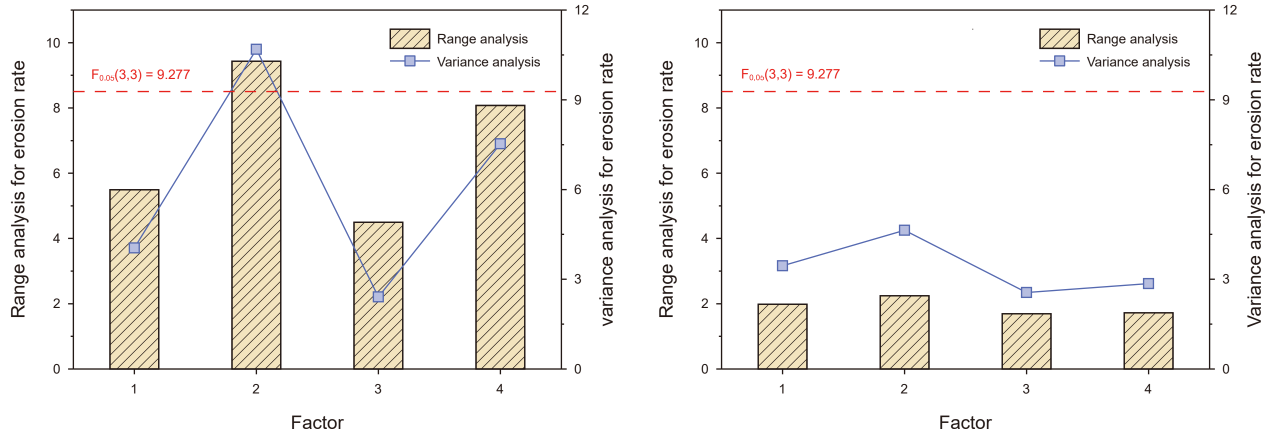


**Fig. 14.** Range and variance analysis of maximum erosion rate of PSS (left) and MWM (right).

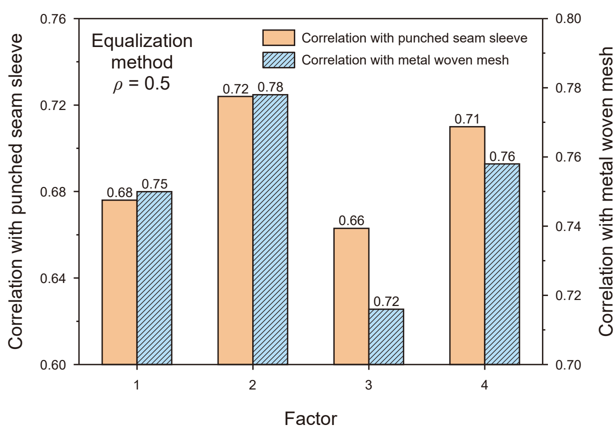


**Fig. 15.** Sorting of the factors by gray correlation analysis method.

The opening height of the PSS is designed according to the particle size distribution of the reservoir and cannot be changed at will. Then, only the specifications and arrangement of the PSS can be optimized. Under the condition of ensuring a certain opening rate, the specifications of the PSS are optimized, and the optimization scheme is shown in Table 10.

### 4.5.2. Analysis of optimization results of PSS

The water content was set to 1%, the velocity was 3 m/s, the particle diameter was 0.05 mm, and the mass flow rate was 0.01 kg/s. For different specifications, the maximum erosion wear cloud diagram of the PSS is shown in Fig. 16(a). The maximum erosion wear cloud diagram of MWM with different specifications is shown in Fig. 16(b). Due to the different width of the PSS, the erosion area of the MWM is different. When the width is 2.64 mm, the erosion area covers one weft yarn. When the width is 3.3 mm, the erosion area covers two weft yarns. The larger the width of the erosion area along the x-axis direction, the greater the drag force, the greater the velocity and the more the number of type III particles.

Inside the PSS, the maximum flow velocity area is at the upper end of the outlet (as shown in Fig. 9). When the inlet area is constant, with the increase of width, the ratio of inlet area to outlet area increases, the continuous phase velocity at the slit increases, the drag force increases, and the maximum erosion rate of the PSS and MWM increases. From 2.64 to 3.30 mm, the maximum velocities of continuous phase are 8.088, 9.526 and 11.518 m/s, respectively.

The particle data of erosion defects are shown in Table 11. From 2.64 to 3.30 mm, the number of particles of erosion defects gradually decreases. When the outlet width increases from 2.64 to 3.30 mm, the average velocity of the particles eroding defect increases in turn, which indicates that the drag force has obvious work on the particles and the velocity increases significantly. The maximum erosion rate of the PSS is positively correlated with the particle velocity, and the influence of the velocity is significantly greater than the number of particles, so the erosion rate of the PSS increases.

Keeping the production pressure difference constant, the influence of different specifications of the punching sleeve structure on the yield was studied. The production rate is calculated by the average flow rate (reference Eq. (8)), and the relationship between relative productivity is obtained (as shown in Table 11).

Near the outlet of the PSS, the effect of the drag force on the particles cannot be ignored, and the velocity of the continuous phase has a significant effect. Reasonable design of the specifications of the PSS and reduction of the velocity of the continuous phase can effectively control the erosion rate of the PSS and MWM, and improve the service life of the sand control screen. According to Tables 10 and 11, the smaller the ratio of the inlet area to the outlet area, the smaller the maximum velocity of the continuous phase, and the smaller the erosion rate of the PSS and MWM. Compared with the original model, Model 2 can greatly reduce the erosion rate of sand control screen and improve the service life of sand control screen (under the condition of ensuring that the output does not decrease).

**Table 10**
Specifications of PSS.

| Model | Specification of PSS, mm | | | Inlet area/outlet area |
|---|---|---|---|---|
| | Longevity | Width | Open height | |
| Original model | 22 | 3 | 0.5 | 3.27 |
| Contrast model 1 | 20 | 3.3 | | 3.63 |
| Contrast model 2 | 25 | 2.64 | | 2.84 |

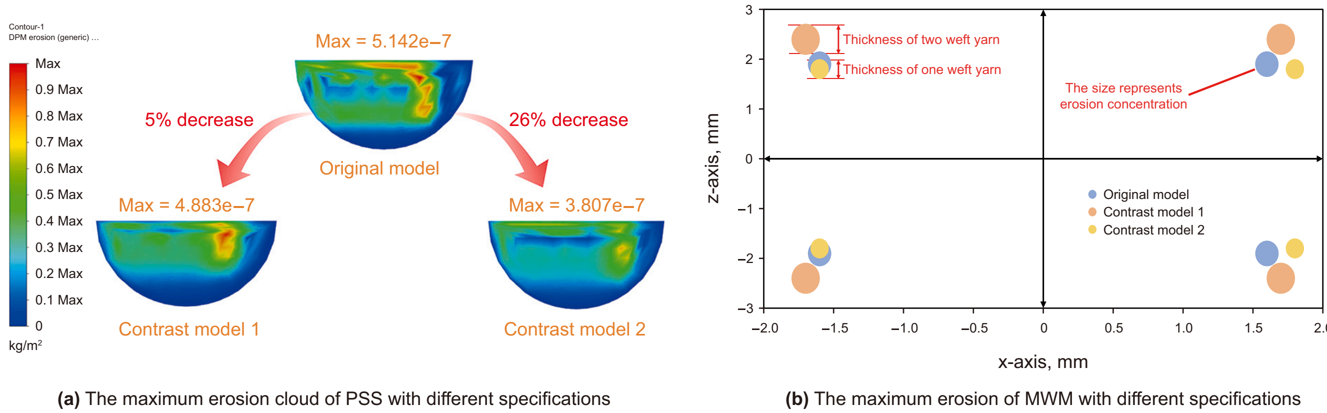


**Fig. 16.** The maximum erosion wear of PSS and MWM with different specifications.

**Table 11**
Numerical simulation results.

| Model | Number of particles | Average velocity, m/s | Relative yield | Maximum dynamic erosion rate, $10^{-5}$ kg/(m$^2$·s) | |
|---|---|---|---|---|---|
| | | | | PSS | MWM |
| Original model | 137071 | 3.094 | 1.000 | 4.413 | 0.466 |
| Contrast model 1 | 122620 | 3.231 | 0.933 | 4.191 | 0.721 |
| Contrast model 2 | 151136 | 2.995 | 1.206 | 3.277 | 0.374 |

## 5. Conclusions

In this paper, the dynamic erosion mechanism of sand control screen is studied by erosion experiment and dynamic numerical simulation, and the corresponding conclusions are obtained.

(1) Based on corrosive environment, the erosion model of three kinds of particles is established. Among them, type I particles directly erode the middle part of the flow channel, type II particles erode the edge of the flow channel, and type III particles directly erode the MWM.
(2) When the water content increases from 0.5% to 7%, the maximum erosion wear of the defect increases first and then decreases, and the maximum erosion wear of the MWM continues to increase. When the gas production rate increases from 3 to 10 m/s, the maximum erosion wear of the defect of PSS and MWM increase exponentially.
(3) In the process of sand control screen erosion, the erosion rate of the PSS is one order of magnitude higher than that of the MWM. In the process of screen structure optimization, priority should be given to how to reduce the erosion rate of the PSS.
(4) Among the factors water content, velocity, particle diameter, mass flow rate, that affect the erosion rate, velocity has the greatest influence on the maximum dynamic erosion rate of the PSS and MWM, and only the velocity has a significant influence on the maximum dynamic erosion rate of the PSS.
(5) According to the research results, the ratio of the inlet area to the outlet area of the PSS is optimized. Compared with the original model, the maximum erosion rate of the optimized model is reduced by 26%, thereby improving the life of the screen pipe.

Based on the characteristics of low sand volume fraction in gas wells, this paper uses CFD-DPM model to study the erosion mechanism. In future studies, other models can be used to study the erosion mechanism of sand control screens containing gravel layers or considering clogging. On the basis of a single PSS unit, the influence of unit distribution on sand control of screen pipe can be considered.

## CRediT authorship contribution statement

**Fu-Cheng Deng:** Funding acquisition, Formal analysis, Data curation, Conceptualization. **Jun Gong:** Writing – review & editing, Writing – original draft, Visualization, Validation. **Ning Gong:** Resources, Project administration, Methodology. **Yao-Tu Han:** Resources, Project administration, Methodology. **Yi-Mou Li:** Writing – original draft, Software.

## Declaration of interest statement

We declare that we do not have any commercial or associative interest that represents a conflict of interest in connection with the work submitted.


## Acknowledgements

This research is supported by Open Fund (PLN2021-14) of State Key Laboratory of Oil and Gas Reservoir Geology and Exploitation (Southwest Petroleum University) and Natural Science Foundation of China (52474031). We thank Yanlong Li and Yongjiang Luo for their help.


## Appendix

*Optimization method of flow channel model.*

The warp and weft intersect at one point. When the software is operated, this point is infinitely small, and it is easy to not converge, so the flow channel model cannot be solved. In order to establish the flow channel model of metal woven mesh, it is necessary to increase the intersection volume of warp and weft or interval a certain distance during modeling.

According to the erosion experiment and simulation results of the metal woven mesh, under the condition of no blockage, the erosion area is mainly distributed on the weft wire and concentrated on the downward bending part. As shown in Fig. A1, the exposed area of the warp is less than 10% of the whole, and the erosion of the warp is small, so the optimization of the warp does not affect the overall characteristics. In actual production, it is impossible to completely close contact between the weft yarns, and the inspection can reach the national standard. When modeling, there is a certain gap between the weft yarns (it is recommended to be less than 10% of the diameter of the weft yarn), but the actual aperture of the model must be guaranteed to meet the national standards.

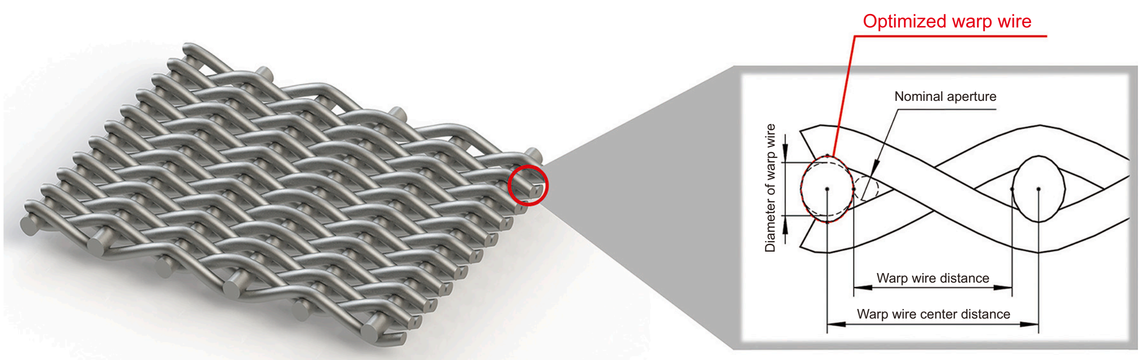


**Fig. A1.** The structure of metal woven mesh.

Fig. A1 shows that a certain diameter of the warp and weft yarns are woven according to the standard, forming a metal woven mesh with a nominal aperture $d_0$. The optimization of the warp must ensure that the nominal aperture $d_0$ remains unchanged, that is, the actual aperture $d_1$ remains unchanged. According to the specifications specified in the national standard, a metal woven mesh model is established, and then a warp wire model with an elliptical cross section is established to cover the original warp wire model, and the optimization of the metal woven mesh model is completed. Finally, the cutting function is used to cut the flow channel model away from the metal woven mesh model, and the flow channel model with the characteristics of the metal woven mesh is established.

## Abbreviations

| | |
|---|---|
| PSS | Punched seam sleeves |
| MWM | Metal woven meshes |
| HPK | High-pressure kettle |
| CFD | Computational fluid dynamics |
| DPM | Discrete phase model |

## References


Abduljabbar, A., Amadi, A., Mohyaldinn, M.E., Ridha, S., Younis, O., Alakbari, F.S., 2024. Sand screens application and performance for sand control: a review of selection criteria, screen materials, and causes of failure. Heliyon 10, e30731. https://doi.org/10.1016/j.heliyon.2024.e30731.

Abduljabbar, A., Mohyaldinn, M., Younis, O., Alghurabi, A., 2021. A numerical CFD investigation of sand screen erosion in gas wells: effect of fine content and particle size distribution. J. Nat. Gas Sci. Eng. 95, 104228. https://doi.org/10.1016/j.jngse.2021.104228.

Akash, F.A., Shovon, S.M., Rahman, MdA., Rahman, W., Chakraborty, P., Haque, MdN., Monir, M.U., Habib, MdA., Biswas, A.K., Chowdhury, S., Khan, M.F.H., Prasetya, T.A.E., 2024. Innovative pathways to sustainable energy: advancements in clean coal technologies in Bangladesh—a review. Clean. Eng. Technol. 22, 100805. https://doi.org/10.1016/j.clet.2024.100805.

Alghurabi, A., Mohyaldinn, M., Jufar, S., Younis, O., Abduljabbar, A., Azuwan, M., 2021. CFD numerical simulation of standalone sand screen erosion due to gas-sand flow. J. Nat. Gas Sci. Eng. 85, 103706. https://doi.org/10.1016/j.jngse.2020.103706.

Amadi, A., Mohyaldinn, M., Ridha, S., 2024. Sand particle induced erosion in oil and gas screens: a review of influencing factors and wear dynamics. Powder Technol. 436, 119528. https://doi.org/10.1016/j.powtec.2024.119528.

Bozzini, B., Ricotti, M.E., Boniardi, M., Mele, C., 2003. Evaluation of erosion–corrosion in multiphase flow via CFD and experimental analysis. 14th Int. Conf. Wear Mater. 255, 237–245. https://doi.org/10.1016/S0043-1648(03)00181-9.

Chen, Y., Yan, C.L., Cheng, Y.F., Han, Z.Y., Li, Y., Xue, M.Y., Wang, T., 2024. DEM-CFD coupling verification and analysis of a sand control medium structure with weakened particle blockage performance. Powder Technol. 441, 119811. https://doi.org/10.1016/j.powtec.2024.119811.

Chen, Yong, Wu, H.C., Chen, Y.J., Li, P.C., Wang, Q.L., 2022. Erosion-corrosion coupling analysis of shale gas production pipe. Eng. Fail. Anal. 138, 106308. https://doi.org/10.1016/j.engfailanal.2022.106308.

Chi, M.H., Zeng, X.G., Gao, Y., Li, W., Jiang, H.Y., Sun, R.C., 2024. The erosion rate prediction for the elbow in shale gas gathering and transportation system: RSM and GA-BP-ANN modeling. Powder Technol. 435, 119429. https://doi.org/10.1016/j.powtec.2024.119429.

Constien, V.G., Skidmore, V., 2006. Standalone Screen Selection Using Performance Mastercurves. Presented at the SPE International Symposium and Exhibition on Formation Damage Control. SPE-98363-MS. https://doi.org/10.2118/98363-MS

Deng, F.C., Li, Y.M., Gong, N., 2024a. Study on dynamic erosion mechanism of punching sleeve in water-producing gas well. Pet. Mech. 52, 82–90 (in Chinese). https:doi.org/10.16082/j.cnki.issn.1001-4578.2024.02.012.

Deng, F.C., Wen, L., Li, G., Fan, B.T., Gong, N., Chen, S.H., 2024b. Study of the blocking mechanism in gravel packing based on CFD-DEM. Particuology 90, 164–178. https://doi.org/10.1016/j.partic.2023.12.005.

Dickenson, J.A., Sansalone, J.J., 2009. Discrete phase model representation of particulate matter (PM) for simulating PM separation by hydrodynamic unit operations. Environ. Sci. Technol. 43, 8220–8226. https://doi.org/10.1021/es901527r.

Ding, J.P., Cheng, Y.F., Yan, C.L., Lu, C., Li, Y., Xue, M.Y., 2021. Numerical simulation on sand production in the exploitation process of gas hydrates based on skeleton failure of reservoirs. J. Nat. Gas Sci. Eng. 94, 104052. https://doi.org/10.1016/j.jngse.2021.104052.

Dong, C.Y., Gao, K.G., Dong, S.X., Shang, X.S., Wu, Y.X., Zhong, Y.X., 2017. A new integrated method for comprehensive performance of mechanical sand control screens testing and evaluation. J. Pet. Sci. Eng. 158, 775–783. https://doi.org/10.1016/j.petrol.2017.08.043.

Dou, X.F., Liu, Z.C., Yang, D.H., Zhao, Y.J., Li, Y.L., Gao, D.L., Ning, F.L., 2025. 3D CFD-DEM modeling of sand production and reservoir compaction in gas hydrate-bearing sediments with gravel packing well completion. Comput. Geotech. 177, 106870. https://doi.org/10.1016/j.compgeo.2024.106870.

Edwards, J., McLaury, B., Shirazi, S., 2000. Evaluation of alternative pipe bend fittings in erosive service. Am. Soc. Mech. Eng. Fluids Eng. Div. Publ. FED 253, 959–966.

Finnie, I., McFadden, D.H., 1978. On the velocity dependence of the erosion of ductile metals by solid particles at low angles of incidence. Wear 48, 181–190. https://doi.org/10.1016/0043-1648(78)90147-3.

Finnie, I., Stevick, G.R., Ridgely, J.R., 1992. The influence of impingement angle on the erosion of ductile metals by angular abrasive particles. Wear 152, 91–98. https://doi.org/10.1016/0043-1648(92)90206-N.

Fu, S.B., Wang, Z.G., Fu, H.P., Shi, J., Zhao, X.F., Meng, L., Wu, J.H., Li, D., 2025. Erosion-corrosion behavior of pipelines for enhanced oil recovery and storage in permafrost. Appl. Therm. Eng. 279, 127527. https://doi.org/10.1016/j.applthermaleng.2025.127527.

Haider, A., 1989. Drag coefficient and terminal velocity of spherical and non-spherical particles. Powder Technol. 58, 63–70. https://doi.org/10.1016/0032-5910(89)80008-7.
Haugen, K., Kvernvold, O., Ronold, A., Sandberg, R., 1995. Sand erosion of wear-resistant materials: Erosion in choke valves. Wear 186–187, 179–188. https://doi.org/10.1016/0043-1648(95)07158-X.
Ismail, N.I., Kuang, S.B., Tang, Y.C., Yu, A.B., 2022. CFD-DEM evaluation of screen types for sand control applications. Powder Technol. 404, 117496. https://doi.org/10.1016/j.powtec.2022.117496.
Jing, J., Tian, Y., Zhu, X.H., Zhou, Y., Shi, C.S., Lei, Q.L., 2024. Safety evaluation of offshore oil and gas well string based on corrosion rate prediction. J. Loss Prev. Process. Ind. 91, 105385. https://doi.org/10.1016/j.jlp.2024.105385.
Li, F.L., Tang, Q., Yan, W., Li, J., Li, W.B., Yang, T., Lin, L., Jiang, K., Wang, K.Y., Zhang, W., 2023. Research on the failure analysis and prediction method of casing deformation under the synergistic effect of sand production and corrosion. Eng. Fail. Anal. 154, 107706. https://doi.org/10.1016/j.engfailanal.2023.107706.
Li, X.H., Tian, F.F., Zhang, R.R., Han, Z.Y., Liu, X.Q., 2025. Dynamic safety assessment of underground compressed air energy storage string subjected to erosion-corrosion degradation. Reliab. Eng. Syst. Saf. 261, 111070. https://doi.org/10.1016/j.ress.2025.111070.
Liu, E.B., Huang, S., Tian, D.C., Shi, L.M., Peng, S.B., Zheng, H., 2024. Experimental and numerical simulation study on the erosion behavior of the elbow of gathering pipeline in shale gas field. Pet. Sci. 21, 1257–1274. https://doi.org/10.1016/j.petsci.2023.08.034.
Mansour, A.A., Aouad, M.R., Al-Sodies, S., Messali, M., El fallah, H., amarray, A., Dahbi, M., Bazzi, L., Salghi, R., Rezki, N., 2025. Dicationic ionic liquids derivatives for advanced corrosion protection of N80 carbon steel: electrochemical, computational and raman spectroscopic studies. J. Mol. Struct., 142240 https://doi.org/10.1016/j.molstruc.2025.142240.
McLaury, B.S., Wang, J.R., Shirazi, S.A., Shadley, J.R., Rybicki, E.F., 1997. Solid Particle Erosion in Long Radius Elbows and Straight Pipes. In: SPE Annual Technical Conference and Exhibition, San Antonio, Texas, October. https://doi.org/10.2118/38842-MS.
Morsi, S.A., Alexander, A.J., 1972. An investigation of particle trajectories in two-phase flow systems. J. Fluid Mech. 55, 193. https://doi.org/10.1017/S0022112072001806.
Oka, Y.I., Matsumura, M., Kawabata, T., 1993. Relationship between surface hardness and erosion damage caused by solid particle impact. Wear 162–164, 688–695. https://doi.org/10.1016/0043-1648(93)90067-V.
Parsi, M., Najmi, K., Najafifard, F., Hassani, S., McLaury, B.S., Shirazi, S.A., 2014. A comprehensive review of solid particle erosion modeling for oil and gas wells and pipelines applications. J. Nat. Gas Sci. Eng. 21, 850–873. https://doi.org/10.1016/j.jngse.2014.10.001.
Procyk, A., Gou, X.J., Marti, S.K., Burton, R.C., Knefel, M., Dreschers, D., Wiegmann, A., Cheng, L.P., Glatt, E., 2015. Sand Control Screen Erosion: Prediction and Avoidance. In: SPE Annual Technical Conference and Exhibition. https://doi.org/10.2118/174837-MS
Safaei, A., Asefi, M., Ahmadi, M., Pourshamsi, T., Baloochestanzadeh, S., Khalilnezhad, A., Riazi, M., 2023. Chemical treatment for sand production control: a review of materials, methods, and field operations. Pet. Sci. 20, 1640–1658. https://doi.org/10.1016/j.petsci.2023.02.013.
Sarkar, S., Zamindar, S., Murmu, M., Mandal, S., Majumdar, G., Banerjee, P., 2023. Importance of corrosion inhibition in oil and gas industries: environmental health and safety for sustainable development of oil as well as gas industries. In: Hashmi, S. (Ed.), Comprehensive Materials Processing, second ed. Elsevier, Oxford, pp. 272–281. https://doi.org/10.1016/B978-0-323-96020-5.00102-3.
Shi, S.Z., Zhang, S.S., Cheng, N., Tian, G., Zeng, D.Z., Yu, H.Y., Wang, X., Zhang, X., 2023. Erosion characteristics and simulation charts of sand fracturing casing perforation. Pet. Sci. 20 (6), 3638–3653. https://doi.org/10.1016/j.petsci.2023.06.001.
Wang, H.Y., Tan, Z., Kuang, S.B., Yu, A.B., 2023. Systematic investigation of centrifugal slurry pump under different operating condition by DDPM method. Powder Technol. 430, 119024. https://doi.org/10.1016/j.powtec.2023.119024.
Wang, T., Chen, S.H., Li, M.L., An, M.K., 2024. A resolved CFD-DEM investigation into sand production under water flooding in unconsolidated reservoir. Powder Technol. 442, 119859. https://doi.org/10.1016/j.powtec.2024.119859.
Wong, G.K., Fair, P.S., Bland, K.F., Sherwood, R.S., 2003. Balancing Act: Gulf of Mexico Sand Control Completions, Peak Rate Versus Risk of Sand Control Failure. In: SPE Annual Technical Conference and Exhibition. https://doi.org/10.2118/84497-MS.
Xie, L., Tang, Y., Wang, J.Z., Wang, J., 2025. Experimental study on the L80 steel column sample of gas storage reservoir tubing in high-pressure three-phase flow: erosion mechanism and impact angle effect. Chem. Eng. Sci. 310, 121490. https://doi.org/10.1016/j.ces.2025.121490.
Yang, Y.X., He, M.Q., Yu, P., Kan, C.B., Wang, X.P., Yu, X.C., Chen, X.Y., Tao, S.L., Zhao, C., Duan, J.B., An, J.Q., Sun, Z.Y., 2024. Investigation on critical erosion of gas production channel for sand carrying during injection and production process in gas storage. Geoenergy Sci. Eng. 239, 212945. https://doi.org/10.1016/j.geoen.2024.212945.
Ye, Z.R., Li, X.S., Shi, S.K., Wang, M., Li, J.N., Zhao, Z.H., Li, S.A., Wang, Y., Sun, J.B., Zhao, W.M., 2025. Influence of H2O phase state on corrosion behavior of Q125 in high-temperature $H_2O$-$CO_2$-$H_2S$-$H_2$ environment. Mater. Chem. Phys. 339, 130800. https://doi.org/10.1016/j.matchemphys.2025.130800.
Zambrano, O.A., Qian, W.M., Jiang, J. (Jimmy), 2025. Slurry erosion of tool steels by large erodent particles. Wear 564–565, 205719. https://doi.org/10.1016/j.wear.2024.205719.
Zeng, D.Z., Zhang, S.S., Li, J., Wang, X., Tian, G., Zhang, X., Yu, H.Y., Li, X.G., 2023. An experimental study on casing perforation erosion during sand fracturing. Wear 528–529, 204980. https://doi.org/10.1016/j.wear.2023.204980.
Zhang, R., Hao, S.Z., Zhang, C., Meng, W.B., Zhang, G.C., Liu, Z.H., Gao, D.L., Tang, Y.N., 2020. Analysis and simulation of erosion of sand control screens in deep water gas well and its practical application. J. Pet. Sci. Eng. 189, 106997. https://doi.org/10.1016/j.petrol.2020.106997.
Zhou, L.C., Huang, X.G., Song, W.J., Huang, C., Liu, H.H., Wang, H.X., 2024. Multi-factor corrosion model of TP110TS steel in H2S/CO2 coexistence and life prediction of petroleum casings. Int. J. Press. Vessels Pip. 209, 105204. https://doi.org/10.1016/j.ijpvp.2024.105204.
Zhu, H.X., Xu, T.F., Yuan, Y.L., Feng, G.H., Xia, Y.L., Xin, X., 2020. Numerical analysis of sand production during natural gas extraction from unconsolidated hydrate-bearing sediments. J. Nat. Gas Sci. Eng. 76, 103229. https://doi.org/10.1016/j.jngse.2020.103229.
Zhu, T., Gong, H.J., Dong, M.Z., 2021. Density and viscosity of $CO_2+$ ethyl acetate binary systems from 308.15 to 338.15 K and 15 to 45 MPa. Fluid Phase Equilib. 537, 112988. https://doi.org/10.1016/j.fluid.2021.112988.